MODEL-BASED CONTROLLER DESIGN FOR ACTIVE GUST LOAD ALLEVIATION OF AN EXPERIMENTAL FLEXIBLE WING

F. Stalla*, T. Kier*, L. Evangelisti*
* Insitute of System Dynamics and Control, German Aerospace Center (DLR), 82234 Weßling, Germany

Abstract

Alleviating gust and maneuver induced loads acting on the wing of a transport aircraft allows to reduce structural weight, which in turn improves fuel economy and environmental friendliness. This is why active load control is being investigated for future aircraft configurations. In this paper the model-based design of a gust load alleviation control law is described. The controller shall be tested in an upcoming wind tunnel experiment, conducted within the oLAF project (optimal load-adaptive aircraft) of the German Aerospace Center (DLR). The oLAF reference configuration is a long-range transport aircraft, with a high aspect ratio swept wing. The aeroservoeolastic modeling uses the VarLoads environment to construct a structural model in the modal domain, coupled with an aerodynamic model employing the doublet lattice method. The Loewner Framework is found to deliver excellent results when applied for gust modeling, as well as for model order reduction. The gust load controller is synthesized using H_∞ optimal control, taking robustness requirements into account. The performance is evaluated in a nonlinear simulation.

Keywords

Gust Load Alleviation; Flexible Wing; Aeroservoelasticity; Loewner Framework; H_∞ control

1. INTRODUCTION

Increasing efficiency and reducing the environmental impact of aircraft is a primary target of the aviation industry. Novel control techniques can contribute to this objective. Due to aerodynamic and structural optimization, aircraft tend to become more and more flexible, making them more susceptible to external disturbances like gusts and dynamic response phenomena. This is why functionalities to control the flexible motion are attracting attention. One area of research is active load control, aiming to reduce the loads induced by maneuvers and gusts. Simultaneously applying gust and maneuver load alleviation can reduce the structural weight of the wing by up to 30% and the fuel consumption by up to 10%, according to [1], [2], [3].

Within the oLAF project† (optimal load-adaptive aircraft) at the German Aerospace Center (DLR), maneuver and gust load alleviation is investigated, with application to a long-range aircraft. A reference configuration is developed [4], featuring a wing with high aspect ratio and sweep. A wind tunnel test shall be conducted to experimentally validate gust load alleviation functionalities. For the wind tunnel test, a scaled model of the oLAF wing is built [5]. A CAD representation (supplied by DLR-AE-LAE§) of this wind tunnel model is shown in figure 1.

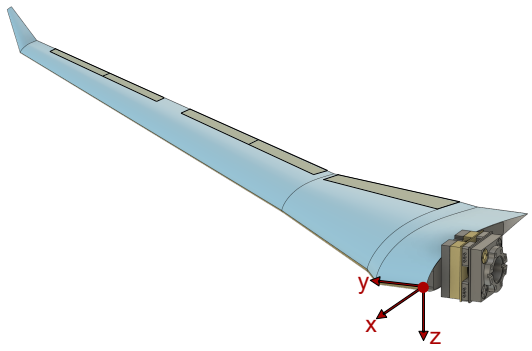

FIG 1. CAD model§ of the oLAF wing wind tunnel model

This paper focuses on the model-based design of a gust load alleviation (GLA) controller to be tested in the oLAF wind tunnel experiment. The controller can command the deflection of five trailing edge control surfaces (see figure 1) to reduce the loads that occur due to a gust acting upon the experimental flexible wing. Ten acceleration sensors distributed across the wing provide information about the current state, these are used for feedback control. The experiment will be conducted at subsonic speeds with a freestream velocity of 50 m/s.

To design the GLA controller, in a first step an aeroservoelastic model of the oLAF experimental wing is created using the VarLoads environment [6], [7]. Aeroservoelasticity indicates that this model contains the structural properties, the aerodynamics, the aero-structural coupling, as well as actuators and sensors of the wing. A nonlinear MATLAB-Simulink simulation is set up. For controller design, a reduced order state-space model is derived from this full order nonlinear model.

One important aspect is how to include the gust disturbance into the model used for controller design. A major challenge is to transform the complex gust aerodynamics from frequency to time domain. Here, the Loewner framework [8] will be applied, yielding very satisfactory results.

Having built the plant model, the controller design itself is conduced applying H_∞ optimal control. This allows to incorporate robustness as well as performance requirements in the design process. The performance and robustness of the developed controller is evaluated, comparing the system with and without gust load alleviation.

2. AEROSERVOELASTIC MODELING

The plant for GLA controller design is the aeroservoelastic model of the experimental flexible wing. The underlying mathematical description of such a system is based on the rigid body and flexible equations of motion (mean axis) [9], [10]. The first equation (b-set) depicts the rigid body dy-

doi: 10.25967/610442

namics around the center of gravity, the second equation the flexible dynamics (f-set). The notation is adapted from the Nastran Aeroelastic Analysis User's Guide [11]. The equations of motion are written in the modal domain:

$$\begin{bmatrix} m_b \cdot (\dot{\mathbf{V}}_b + \boldsymbol{\Omega}_b \times \mathbf{V}_b - \mathbf{T}_{bE} \cdot \mathbf{g}_E) \\ \mathbf{J}_b \cdot \dot{\boldsymbol{\Omega}}_b + \boldsymbol{\Omega}_b \times (\mathbf{J}_b \cdot \boldsymbol{\Omega}_b) \end{bmatrix} = \boldsymbol{\Phi}_{gb}^T \cdot \mathbf{P}_g^{ext}, \tag{1}$$

$$\mathbf{M}_{ff} \cdot \ddot{\mathbf{u}}_f + \mathbf{B}_{ff} \cdot \dot{\mathbf{u}}_f + \mathbf{K}_{ff} \cdot \mathbf{u}_f = \boldsymbol{\Phi}_{gf}^T \cdot \mathbf{P}_g^{ext}.$$

The rigid and flexible modes are excited by external forces on the structural set $\mathbf{P}_g$, fed through the eigenvector matrix $\boldsymbol{\Phi}_{gb}$ and $\boldsymbol{\Phi}_{gf}$. The external forces are created by aerodynamics and the gust disturbance and stand on the right side of the equations of motion. The mass m_b, inertial tensor $\mathbf{J}_b$, modal matrices of mass $\mathbf{M}_{ff}$, damping $\mathbf{B}_{ff}$ and stiffness $\mathbf{K}_{ff}$ are describing the structural part of the oLAF model. The motion itself is captured using the modal deflection $\mathbf{u}_f$, rigid body linear velocity $\mathbf{V_b}$, rotational velocity $\boldsymbol{\Omega}_b$ and their derivatives.
Compared to a free-flying aircraft a wind tunnel model is fixed to the wall. Thus, the rigid body motion does not develop freely driven by the external forces. Instead, the orientation, rate and acceleration can be imposed. This in turn creates forces acting on the flexible model. Other than the pitch, no rigid body motion is represented in the oLAF wind tunnel experiment.
The force summation method [12] is used to recover the loads, which shall be minimized by the GLA (neglecting the influence of damping on the loads):

$$\begin{aligned} \mathbf{P}_g^{FSM} &= \mathbf{P}_g^{ext} - \mathbf{P}_g^{inertia} \\ &= \mathbf{P}_g^{ext} - \mathbf{M}_{gg} \cdot (\boldsymbol{\Phi}_{gb} \cdot \ddot{\mathbf{u}}_b + \boldsymbol{\Phi}_{gf} \cdot \ddot{\mathbf{u}}_f). \end{aligned} \tag{2}$$

The wind tunnel experiment will be carried out at subsonic speeds, with a freestream velocity of $U_\infty = 50\ m/s$ and $M = 0.15$, at ISA sea level values for pressure, density and temperature.

2.1. Structural model

The structural model provides the matrices on the left side of equation 1. A finite element model of the oLAF wind tunnel wing is set up by DLR-AE-LAE[§]. To reduce the size of the resulting model, a Guyan reduction [13] is applied to condense the model to a beam representation. The structural nodes of the condensed model lie along the loads reference axis. To further reduce the size of the matrices, a modal truncation [14] is applied, taking only the first 15 flexible modes into account.
The wind tunnel model exhibits a high torsional rigidity, which is why the first six modes are bending-related. The first torsional mode appears at the seventh lowest eigenfrequency. The first bending mode occurs at a frequency of about 50 rad/s in the undamped system without aerodynamic contribution.
As stated previously, the rigid body motion is not modeled as for a free-flying aircraft. The pitching motion can be imposed at the wind-tunnel mount. The resulting forces on the structural set are computed at the center of gravity and then fed into the flexible part of the equations of motion.

2.2. Aerodynamic model

The equations of motion are driven by the external forces, on the right side of equation 1. Aerodynamics are the main contribution to these forces. The doublet lattice method (DLM) [15], [16] is used to calculate steady and unsteady aerodynamic forces. It is evaluating the unsteady Prandtl-Glauert equation [17]. Since the oLAF experiment is carried out at low speeds ($M = 0.15$), this aerodynamic method based on potential flow theory is sufficient, keeping computational effort moderate.
For application of the DLM the wing is discretized into panels. The result of the DLM is an aerodynamic-influence-coefficient (AIC) matrix $\mathbf{Q}_{jj}$, linking the downwash w_j at the quarter-chord point of each panel to the pressure coefficient of the respective panel Δc_p [15]. A pressure-to-load-matrix $\mathbf{S}_{kj}$ [9] transforms the pressure difference into a force at the reference point. Since the DLM is a frequency domain method, the following equation for a specific reduced frequency k [18] results [9]:

$$\mathbf{P}_k^{aero}(k) = q_\infty \cdot \mathbf{S}_{kj} \cdot \mathbf{Q}_{jj}(k) \cdot \mathbf{w}_j \tag{3}$$

The downwash $\mathbf{w}_j$ on each panel can be induced by the flexible motion of the wing, the rigid body motion, or a deflection of the control surfaces. Thus, a coupling between structural and aerodynamic model needs to be established, as presented in the subsequent section.

2.3. Aero-Structural Coupling

The coupling between aerodynamic and structural model is performed in two steps, as this best allows to capture the structural behavior of the wing. The structural grid points are located along a beam axis (loads reference axis). In a first step a rigid body spline [19] is used to map the motion of the structural grid points from the beam axis to the end points of spars running in chordwise direction. These spars exhibit a high torsional rigidity, which is why a rigid attachment is a suitable modeling approach. Secondly, from the beam as well as the spar end points a mapping onto the aerodynamic panels is performed. A radial basis function approach using an infinite plate spline [20] is employed. Both splining steps are summarized in the matrix $\mathbf{T}_{kg}$. For the inverse coupling, transferring forces from the aerodynamic to the structural model, the transposed matrix is used. Additionally, a mapping from the control surface orientation (x-set) to the orientation of the aerodynamic panels is required. The matrix $\mathbf{T}_{kx}$ is created from a purely geometric relation.
Figure 2 presents the resulting aero-structural model. The aerodynamic discretization for the DLM is shown. The five trailing edge control surfaces that are used for load alleviation are marked. The structural grid points of the condensed model are indicated by diamonds.

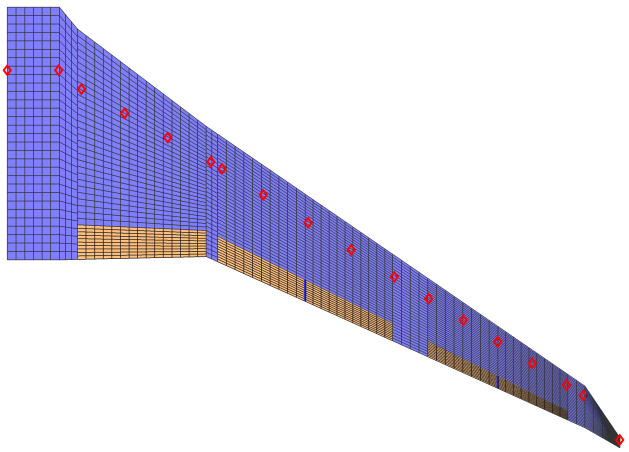

FIG 2. Aero-structural model with discretization from the DLM

Having completed the aero-structural coupling, the aerodynamic contribution to the external forces can be stated - still in the frequency domain for a certain reduced frequency:

$$\mathbf{P}_g^{aero}(k) = q_\infty \cdot \mathbf{T}_{kg}^T \cdot \mathbf{S}_{kj} \cdot \mathbf{Q}_{jj}(k) \cdot \mathbf{w}_j. \tag{4}$$

with contributions from flexible (f-set, modal domain), rigid body (b-set) and control surface motion (x-set):

$$\begin{aligned} \mathbf{w}_j = &\left(\mathbf{D}_{jk}^1 + i \cdot k \cdot \mathbf{D}_{jk}^2\right) \cdot \mathbf{T}_{kg} \cdot \mathbf{\Phi}_{gf} \cdot \mathbf{u}_f \\ + &\left(i \cdot k \cdot \mathbf{D}_{jk}^2\right) \cdot \mathbf{T}_{kg} \cdot \mathbf{\Phi}_{gb} \cdot \mathbf{u}_b \\ + &\left(\mathbf{D}_{jk}^1 + i \cdot k \cdot \mathbf{D}_{jk}^2\right) \cdot \mathbf{T}_{kx} \cdot \mathbf{u}_x. \end{aligned} \tag{5}$$

2.4. Rational Function Approximation

To construct a simulation model, the aerodynamic forces described by equations 4 and 5 need to be transferred from the frequency to the time or state-space domain. However, the terms in above's equations are not (easily) transferable, there does not exist any suitable Laplace or Fourier transform. Therefore, the equation terms are firstly approximated in the frequency domain, to make them suitable for a Laplace transform, and secondly transformed. Here, a rational function approximation (RFA) is employed, more specifically the method developed by Roger [21], [22]. The RFA can be performed on any AIC matrix. Here, a so-called physical RFA first introduced in [9] is conducted, approximating the matrix $\mathbf{Q}_{gj} = \mathbf{T}_{kg}^T \cdot \mathbf{S}_{kj} \cdot \mathbf{Q}_{jj}$ instead of $\mathbf{Q}_{jj}$:

$$\begin{aligned} \mathbf{Q}_{gj}(ik) &\approx \mathbf{Q}_{gj}^0 + \mathbf{Q}_{gj}^1 \cdot ik + \mathbf{D} \cdot (ik \cdot \mathbf{I} - \mathbf{R})^{-1} \cdot \mathbf{E} \cdot ik, \\ \mathbf{D} &= \begin{bmatrix} \mathbf{Q}_{gj}^3 & \mathbf{Q}_{gj}^4 & \cdots & \mathbf{Q}_{gj}^{n_p+2} \end{bmatrix}, \\ \mathbf{R} &= \mathrm{diag}\left(\begin{bmatrix} -p_1\mathbf{I}_{n_j} & \cdots & -p_{n_p}\mathbf{I}_{n_j} \end{bmatrix}\right), \\ \mathbf{E} &= \begin{bmatrix} \mathbf{I}_{n_j} & \cdots & \mathbf{I}_{n_j} \end{bmatrix}^T. \end{aligned} \tag{6}$$

The physical RFA has the advantage that steady and unsteady aerodynamic contributions can be distinguished. A number of poles p_i has to be chosen, here $n_p = 8$. Applying the RFA, Laplace transforming equation 6 and combining it with equation 4 leads to the aerodynamic forces in the time domain [9]:

$$\begin{aligned} \mathbf{P}_g^{aero}(t) &= q_\infty \cdot \left(\mathbf{Q}_{gj}^0 \cdot \mathbf{w}_j\right) \\ &+ q_\infty \cdot \left(\mathbf{Q}_{gj}^1 \cdot \left(\frac{c_{ref}/2}{U_\infty}\right) \cdot \dot{\mathbf{w}}_j + \mathbf{D} \cdot \mathbf{x}_L(\dot{\mathbf{w}}_j)\right), \\ \dot{\mathbf{x}}_L &= \mathbf{R} \cdot \left(\frac{U_\infty}{c_{ref}/2}\right) \cdot \mathbf{x}_L + \mathbf{E} \cdot \dot{\mathbf{w}}_j. \end{aligned} \tag{7}$$

In this equation, the vector $\mathbf{x}_L$ describes the aerodynamic lag-states [23]. The AIC matrix with superscript 0 models the quasi-steady aerodynamic contribution, the matrix with superscript 1 the added mass term. An acceleration term is not present in the physical RFA [9]. The input to the equation is the downwash $\mathbf{w}_j$ and its derivative, as introduced in equation 5, with ik being equivalent to a time derivative.
The RFA concludes the aero-structural modeling. Additional external forces are created by the gust. How these are computed is treated in section 3. The aero-structural model can now be cast in state-space form or implemented within a simulation.

2.5. Actuators and Sensors

The contribution to the aerodynamic forces are denoted in equation 5. The effect of the flexible motion is captured within $\mathbf{u}_f$, which itself is computed by solving the equation of motion (equation 1). The rigid body motion $\mathbf{u}_b$ is imposed at the model mount. Still to be modeled is the action of the control surfaces $\mathbf{u}_x$, which are moved by actuators.
The actuator dynamics need to be integrated in the model, as these have considerably effects on the performance of the GLA controller. Based on a commanded control surface deflection, the actuator model outputs actual deflection, rate and acceleration. A typical modeling of actuators is a first or second order transfer function [24]. On the oLAF wind tunnel model electromechanical actuators are used. Here, the actuator modeling is adapted from the one performed in a previous DLR wind tunnel project [25]. A first order transfer function was found sufficient to capture the dynamics, more information is available in [26]. All five control surfaces will be equipped with the same actuators.
In the simulation, nonlinearities of the actuation system are taken into account. [24] lists typical nonlinearities introduced by actuators. Here, only the saturation and the dead time will be taken into account. Actuators are assumed to be similar to the experiment analyzed in [26], such that the values are adopted from this paper. The saturation on control surface deflection is 10°, the one on rate is 1129°/s and the dead time is 4.3 ms.
Ten acceleration sensors capturing the motion of the flexible wing are used for feedback within the GLA control loop. The sensors are distributed across the wing. Two sensors are always placed on the same spanwise position, one near the leading and the other near the trailing edge. This allows to capture torsion, while the spanwise distribution allows to capture bending. Figure 3 presents the location and numbering of the acceleration sensors, as well as the one of the control surfaces.

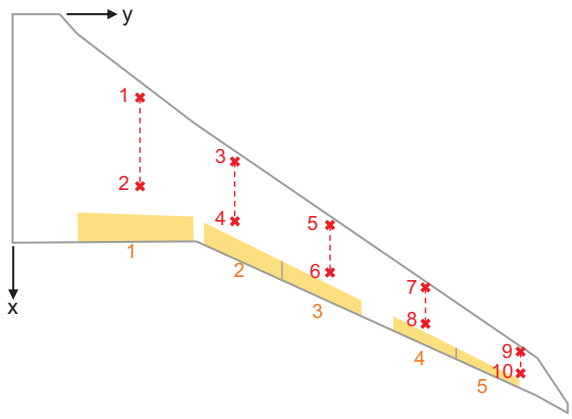

FIG 3. Location of control surfaces and sensors

The sensor dynamics are sufficiently fast to not model them in more detail. Only a dead time of 3 ms [27] will be considered. In the aeroservoelastic model, the sensor measurements are obtained from the acceleration $\ddot{\mathbf{u}}_g$ of the structural grid points by splining. The spline matrix is denoted $\mathbf{T}_{mg}$, where m denotes measurements. From the modal acceleration, the structural acceleration can be computed by multiplying with the eigenvector matrix $\mathbf{\Phi}_{gf}$. Thus, the sensor acceleration is recovered by a pure algebraic computation on the output of the flexible equation of motion.
Including actuators and sensors completes the aeroservoelastic modeling. Next, the gust disturbance needs to be added to the model.

3. GUST MODELING

To synthesize and to validate the controller it is essential to include the gust disturbance into the model. The model should describe the effect of a gust on the flexible wing, i.e. which forces are created due to a gust with a certain length and amplitude interacting with the wing. For the simulation, the gust has to be modeled in the time domain. Starting with frequency domain aerodynamics, the transfer to the time domain cannot be performed with an RFA as outlined in section 2.4. The RFA is unsuited to approximate the AIC column of a gust [28], due to the spiral pattern (when plotting real over imaginary part for multiple reduced frequencies) of the underlying Sears function [23]. To overcome this challenge, the Loewner framework is applied for the task of identifying a state-space model based on a frequency domain representation of the gust aerodynamics.

3.1. Gust Model in the Frequency Domain

The wind tunnel model shall be exposed to discrete 1-cos gusts, as defined in the certification documents CS25 [12]. The downwash induced by a discrete gust can be described using the gust gradient H, the gust amplitude U_{ds}, and the gust start time t_s, as detailed in [12]:

$$w^G(t) = \begin{cases} 0 & t < t_s \\ \frac{U_{ds}}{2 \cdot U_\infty} \cdot \left(1 - \cos\left(\frac{2\pi \cdot U_\infty \cdot t}{2 \cdot H}\right)\right) & t_s \leq t \leq t_e \\ 0 & t > t_e. \end{cases} \tag{8}$$

For the wind tunnel experiment, the gust gradient H - half the gust length - has to be scaled down, using the geometric scale of the model. While for full aircraft the gust gradient ranges between 9 and 107 m, for the oLAF experiment the range is from 0.45 to 5.35 m. The gust amplitude depends on the gust gradient and parameters like the weight of the aircraft, for details see [12]. Figure 4 represents the range of gusts that will be relevant for the oLAF experiment, with the according gust amplitude.

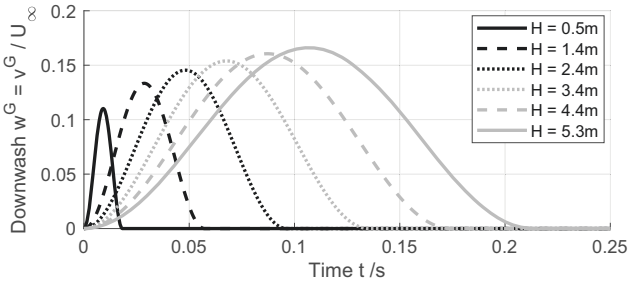

FIG 4. Gust profiles used in the oLAF experiment

Analogously to the aerodynamics due to the motion of the wing itself, the gust aerodynamics can be computed by the DLM in the frequency domain. The following equation taken from [9] holds, with k_G being the reduced gust frequency:

$$\begin{aligned} \mathbf{P}_g^G(k_G) &= q_\infty \cdot \mathbf{Q}_g^G(k_G) \\ &= q_\infty \cdot \mathbf{Q}_{gj}(k_G) \cdot \mathbf{w}_j^G(k_G) \\ &= q_\infty \cdot \mathbf{T}_{kg}^T \cdot \mathbf{S}_{kj} \cdot \mathbf{Q}_{jj}(k_G) \cdot \mathbf{w}_j^G(k_G), \\ \mathbf{w}_j^G(\omega_G) &= \nu_G(\omega_G) \cdot e^{\left(-i\omega_G \cdot \frac{\mathbf{x}_j}{U_\infty}\right)} \cdot \mathbf{n}_j. \end{aligned} \tag{9}$$

The gust loads are calculated by multiplying the AIC matrix with the downwash created by the gust at each panel. This downwash is computed based on an exponential function describing the transport delay with the location x_j of the respective panel (j-set, three-quarter-chord point). The gust spectrum ν_G can be set identical to one, meaning each frequency of gust occurs with the same magnitude, and each frequency is able to contribute to a gust (principle of superposition).

As for the aerodynamic loads, the gust loads contribute to the right side of the equation of motion (equation 1). To transform the gust loads from frequency to time domain, the RFA is not suited [28]. Rational functions are unable to correctly approximate the frequency response of the gust aerodynamics, which are governed by the Sears function [23]. If the gust aerodynamics shall be represented correctly in the time domain, a different approximation method has to be found. Here, the Loewner framework is used to create a state-space model describing the gust dynamics. This approach produces very satisfactory results, and was already applied in for example [28] or [29].

3.2. Loewner Framework for Gust State-Space Model

The Loewner framework can be used both for system identification and for model order reduction. The method is introduced in [8], and further explained in [30]. At the core of the framework is the Loewner and shifted Loewner matrix, which is where the name comes from.

The Loewner framework is supplied with frequency domain data of the AIC gust column $\mathbf{Q}_g^G$ from equation 9 in the form of $\{s_i, \mathbf{Q}_{g,i}^G(s_i)\}$, $i = 1 \ldots n$, where s_i indicates one frequency. A sufficiently large number of frequency data pairs must be supplied, here $n = 1000$ was used. The Loewner framework which is based on tangential interpolation then identifies the underlying system dynamics and returns a state-space system in descriptor form. A design choice when using the Loewner framework are the tangential directions [30]. Selecting these allows to concentrate the system identification on a certain frequency range. Gaussian random numbers (with a fixed seed to ensure reproducibility) delivered the best results, as suggested by [31]. During the identification, a singular value decomposition is performed on the Loewner and shifted Loewner matrix. The number of singular values to be taken into account determines the size of the resulting state-space system. Here $k = 25$ singular values are used, yielding a state-space system of order 25 which approximates the frequency domain data sufficiently accurate.

The resulting state-space system in descriptor form can be transferred to a regular system by inverting the left-side $\mathbf{E}$-matrix. This necessitates it being invertible (non-singular). The system then has the gust column as output, while the input is the one-dimensional gust interacting with the wing:

$$\begin{aligned} \dot{\mathbf{x}}^G &= \mathbf{E}_{gust}^{-1} \cdot \mathbf{A}_{gust} \cdot \mathbf{x}^G + \mathbf{E}_{gust}^{-1} \cdot \mathbf{B}_{gust} \cdot w^G(t), \\ \mathbf{P}_g^G(t) &= q_\infty \cdot \mathbf{C}_{gust} \cdot \mathbf{x}^G. \end{aligned} \tag{10}$$

The input $w^G(t)$ of the system is the gust described by equation 8. The matrices of the resulting state-space system are real, this is guaranteed by a transformation within the Loewner framework, see [30].

3.3. Stabilization of the Loewner Identified System

Depending on the number of singular values used for the gust state-space system (equation 10), the system might be unstable. For usability within simulations and controller design all systems must be stable, meaning any poles in the right complex half plane must be avoided. Koehler [32] proposed a H_2 or H_∞ optimal approach for stabilizing the

system. Following the procedure reveals that the optimal stabilized system can be obtained by omitting the unstable poles entirely. However, this alters the frequency response significantly. Another approach is proposed by Ionita [31]. The sign of the real part of the unstable poles is inverted. Thereby, only the real part is changed while the imaginary part remains the same. This approach is used here. Real matrices are ensured by the same transformation procedure as in the Loewner framework itself, detailed in [30].
After the stabilization by mirroring the unstable poles on the imaginary axis, the frequency response shall be corrected. Since only the real part is altered, this can be achieved by adding a feedthrough matrix. Equation 10 shows no feedthrough matrix. By adding the steady-state difference between unstable and stabilized system, a $\mathbf{D}$-matrix is generated, and the steady-state solution of the stabilized system is corrected. Restoring the correct steady-state frequency response is important for the aerodynamic contribution. Finally, this yields:

$$\begin{aligned} \dot{\mathbf{x}}^G_{stab} &= \mathbf{A}_{gust,stab} \cdot \mathbf{x}^G_{stab} + \mathbf{B}_{gust,stab} \cdot w^G(t), \\ \mathbf{P}^G_g(t) &= q_\infty \cdot \mathbf{C}_{gust} \cdot \mathbf{x}^G_{stab} + q_\infty \cdot \mathbf{D}_{gust,stab} \cdot w^G(t). \end{aligned} \tag{11}$$

It shall be noted that an unstable system identified by the Loewner framework can be avoided by selecting the order high enough. A bisection can be performed to determine the minimum order for stability. However, the aim in this paper was to create a gust state-space system with low order to keep the size of the overall aeroservoelastic model as low as possible.

3.4. Approximation Results

Applying the Loewner framework to identify a gust loads state-space system proves very successful. One can compare the approximated loads with the original loads using a time domain simulation. The former are computed using the state-space system of equation 11, the latter calculated by supplying equation 7 with equation 8. The comparison is shown in figure 5. The gust loads are mapped into the modal domain by pre-multiplying the eigenvector matrix. In the figure only the first four generalized forces are presented.

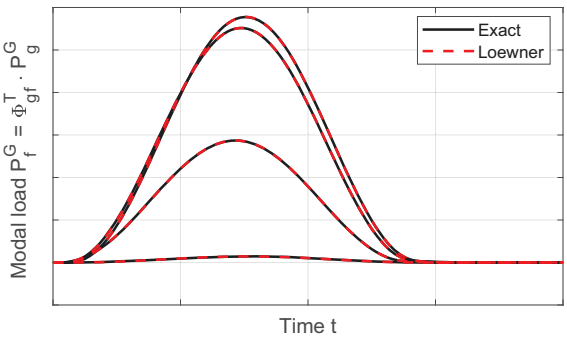

FIG 5. Comparison of modal loads time response due to a gust

There is virtually no difference between original and approximated loads, confirming the excellent approximation achieved with the Loewner framework. These kind of results are achieved for all gust gradients relevant for the oLAF experiment. Besides the time response, the approximation can also be compared to the original loads in the frequency domain, which is done in figure 6. The first entry of the AIC gust column $\mathbf{Q}^G_g$ from equation 7 mapped to the modal domain, i.e. $\mathbf{Q}^G_{f,1}$, is shown. By plotting real over imaginary part, the spiraling behavior of the gust dynamics becomes apparent, similar to the Sears function as presented in [23]. The Loewner approximation is capable of reconstructing this behavior very well.

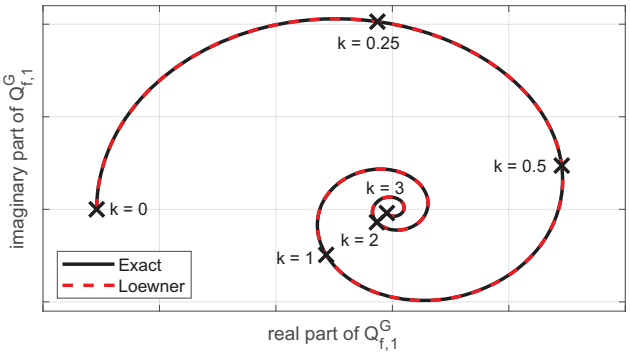

FIG 6. Comparison of the first entry of the AIC gust column

When comparing the results achieved with the Loewner framework to those achieved with an RFA, the superior approximation characteristics of the former become evident. The Loewner framework is a beneficial addition to the aeroservoelastic modeling.

4. MODEL ASSEMBLY AND ORDER REDUCTION

Finally, all the model ingredients can be combined in the overall aeroservoelastic model of the oLAF wind tunnel wing. Two types of models are being created:
1) nonlinear simulation model for time domain simulations and controller validation,
2) linear state-space model for controller synthesis.

4.1. Nonlinear Simulation Model

The simulation model is created in MATLAB-Simulink. The simulation solves the linear elastic equation of motion (equation 1) for acceleration, being supplied with the external forces from aerodynamics (equation 7 with equation 5), from gusts (equation 11), and from the imposed rigid body motion. Integrating the acceleration leads to the rate and displacement of the flexible modes. Actuator and sensor transfer functions are added. Control surface and actuator limits on deflection, rate and acceleration, as well as the overall delay of 8 ms in the servo loop are included. The option to introduce measurement noise is available.
For the evaluation as well as the design of the GLA controller it is important to quantify the loads. The force summation method is used to recover the loads acting on the wing, as presented in equation 2. Cut loads are calculated between the nodes of the condensed structural model. The wing root loads are the cut loads between the innermost and the second structural grid point. Wing-root bending (WRBM) and wing-root torsion moment (WRTM) are the most important loads for the GLA controller.

4.2. Adaptation for the Linear State-Space Model

The linear state-space system is used for controller design. The linearization is performed around a typical cruise angle of attack of 3°, the freestream velocity is 50 m/s as previously mentioned. To construct the state space model, a different RFA is needed as the one presented in equation 7. This is necessary because the internal states of the system are not composed of the downwash on the aerodynamic

panels, but the modal deflection and rate. Using a transformation detailed in [9] one can obtain the RFA matrices mapping from modal to structural set (subscript gf):

$$\mathbf{P}_g^{aero,f} = q_\infty \cdot \mathbf{Q}_{gf}^0 \cdot \mathbf{u}_f + q_\infty \cdot \left(\frac{c_{ref}/2}{U_\infty}\right) \cdot \mathbf{Q}_{gf}^1 \cdot \dot{\mathbf{u}}_f + q_\infty \cdot \left(\frac{c_{ref}/2}{U_\infty}\right)^2 \cdot \mathbf{Q}_{gf}^2 \cdot \ddot{\mathbf{u}}_f + q_\infty \cdot \mathbf{D}_{gf} \cdot \mathbf{x}_{L,f}(\dot{\mathbf{u}}_f),$$

$$\dot{\mathbf{x}}_{L,f} = \mathbf{R}_f \cdot \left(\frac{U_\infty}{c_{ref}/2}\right) \cdot \mathbf{x}_{L,f} + \mathbf{E}_f \cdot \dot{\mathbf{u}}_f.$$

The aerodynamic lag states are also converted. The transformation is equivalently carried out for the control surface and rigid body motion. Integrating this alternative computation of the aerodynamic forces due to the flexible and control surface motion into the equation of motion results in the overall state-space system. The inputs are the gust disturbance w^G, the rigid body motion $\mathbf{u}_b$, $\dot{\mathbf{u}}_b$, $\ddot{\mathbf{u}}_b$ as well as the control surface command $\mathbf{u}_{x,cmd}$ for all five control surfaces, which will later be supplied by the controller. The outputs are the sensor measurements as described in section 2.5, as well as the wing-root cut-loads (WRBM, WRTM). The resulting state-space system therefore has 273 internal states, 25 inputs and 12 outputs.

4.3. Model Order Reduction

For the H_∞ control design method chosen here, the order of the plant model plays an important role, because the controller will have as many states as the plant. Thus, it is necessary to reduce the order of the state-space system used for controller synthesis. Applying balanced truncation [33], [34] is a common choice. Here, the Loewner framework is employed once again. This time, the frequency domain pairs are supplied for the entire transfer function of the state-space model. To improve the quality of the reduction, the input-output-paths are reduced by eliminating the rigid body motion. By selecting the number of singular values used in the Loewner identified descriptor state-space system, the order of the reduced system can be set. The application of the Loewner framework is analogue to the one described in section 3, this time with an order of 50, and with frequency data pairs supplied between $k = 0$ and $k = 1.0$. Stabilization and steady-state correction is also applied.
The reduced order model matches the full order model quite well in the lower frequency domain. The approximation error increases with increasing frequency. Figure 7 compares the relative magnitude of the difference in singular values between full and reduced order model. Below 100 rad/s the error is less than 40 dB, which is satisfactory. The high frequency dynamics are less important for the GLA functionality, due to the roll-off in actuator dynamics.

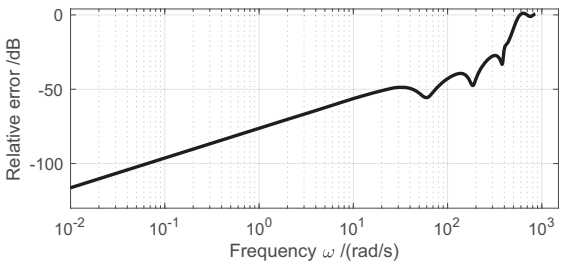

FIG 7. Relative error between full and reduced order model

Figure 7 illustrates the capability of the Loewner framework for model order reduction. Increasing the order of the reduced system would reduce the approximation error, but for controller design a lower order of the plant is favorable.

5. CONTROLLER DESIGN

The aeroservoelastic model in form of the reduced linear state-space model is now used as the plant for model-based controller design. The GLA functionality will be designed using H_∞ optimal control, which is applicable to multiple input multiple output (MIMO) systems [35]. This robust design method allows to incorporate not only performance but also robustness requirements into the controller synthesis. Ensuring stability margins and robustness is an important aspect for the GLA controller, because the plant model contains errors due to assumptions, neglected dynamics, external disturbances and changing operating conditions in the wind tunnel. Robustness ensures that the controller still works even if the modeled plant is not exactly matched by the real experiment.
The standardized form of the H_∞ control loop is shown in figure 8. The generalized plant $\mathbf{P}$ - in which the aeroservoelastic plant is contained together with weighting functions - receives exogenous inputs $\mathbf{w}$ and produces exogenous outputs $\mathbf{z}$. The feedback loop with the controller $\mathbf{K}$ is closed using feedback variables $\mathbf{v}$ which are translated into control commands $\mathbf{u}$.

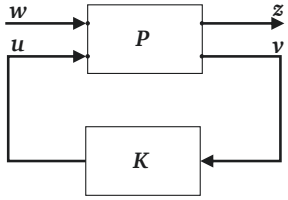

FIG 8. Standard H_∞ control framework, adapted from [35]

The generalized plant $\mathbf{P}$ as shown in figure 8 must be constructed to achieve the control targets, which is why these need to be defined in a first step.

5.1. Control Targets for Gust Load Alleviation

The gust load alleviation shall fulfill the following targets:
1) reduce the integral loads at the wing root, focusing on bending (WRBM) and torsion moment (WRTM),
2) ensure closed loop stability,
3) ensure robustness with respect to modeling errors, neglected dynamics, and changing operating conditions,
4) work for the entire range of gust gradients defined,
5) minimize control activity and avoid steady-state deflections of the control surfaces.

Obviously, these control targets are conflicting and pose a trade-off problem. The first target is a performance target. It is chosen to focus on integral loads on the wing root. A detailed loads analysis to define the critical cases within the envelope of the reference aircraft - then transferred to the wind tunnel experiment - is recommended for future work. The second target demands closed loop stability, which is mandatory for a usable load alleviation. Additionally, the controller itself should also be stable, which is not automatically guaranteed by H_∞ synthesis [35]. Robustness is a more stringent requirement than stability itself, enforcing certain margins before instability occurs.
The fourth target demands that the GLA functionality is usable for the entire range of gust gradients to appear, as determined in section 3.1 between 0.5 and 5.3 m. For the wind tunnel wing, the most critical gust is the one with the longest gradient and accordingly the highest amplitude U_{ds}. In a full aircraft this might be different, because the aircraft

can respond with a rigid body motion if long gusts occur. In the wind tunnel experiment, the wing is clamped, meaning every gust - even a very slow one - leads to a flexible deformation of the wing. The fifth objective is necessary to ensure the practicability of the controller.

5.2. Generalized Plant

The generalized plant is composed to fulfill the control targets defined previously. This means, the exogenous inputs and outputs need to be selected and weighted such that the H_∞ synthesis delivers the desired results. The exogenous input $\mathbf{w}$ will be the gust disturbance w^G interfering with the wing, the exogenous outputs $\mathbf{z}$ are selected as follows:

1) $\mathbf{z}_1$: performance output, from the gust to the wing-root loads $\mathbf{P}_{perf} = [P_{WRBM}, P_{WRTM}]^T$,
2) $\mathbf{z}_2$: robustness output, uncertainty attenuation in the high frequency regime,
3) $\mathbf{z}_3$: control output, minimization of control energy.

The aeroservoelastic plant composed in sections 2 to 4 features wing-root loads and acceleration sensor measurements as outputs. The former are used for the performance output $\mathbf{z}_1$, this will govern the controller design in the lower frequency regime. The robustness output will be using the sensor measurements, and will govern the higher frequency domain. The sensor measurements are also used as feedback variables $\mathbf{v}$. The third exogenous output will focus on weighted control commands.
For the trade-off between performance and robustness, another exogenous input is added: a disturbance $\mathbf{d}$ on the sensor measurements. The higher the value d of the disturbance input, the more focus on robustness. Figure 9 presents the generalized plant, with $\mathbf{H}$ indicating selection matrices and $\mathbf{w}_i$ indicating weighting functions. The reference command is zero, since no deflection around the linearization state is desired when a gust acts.

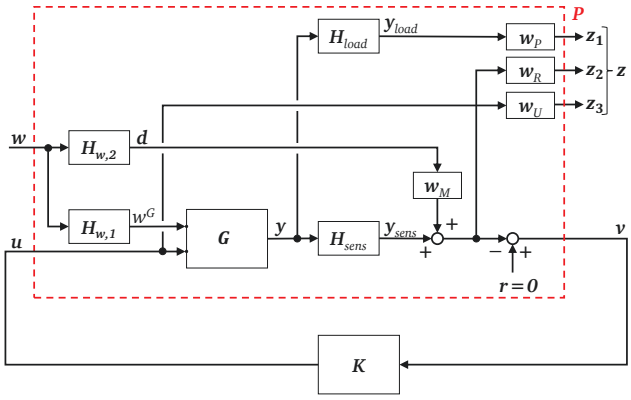

FIG 9. Generalized plant for gust load alleviation control

Selecting the weighting functions to fulfill the desired control targets is an iterative process. Figure 10 presents the weights in their final iteration.
The performance weight $\mathbf{w}_P$ is chosen such that gust loads are reduced in the lower frequency domain. The focus is on the wing-root bending moment, the torsion moment is not as important, since it features a significantly lower magnitude. Thus, the WRBM output is weighted fives times as much as the WRTM. A roll-off to low frequencies avoids the controller trying to reduce steady-state loads. Since the wing is clamped, the low frequent and steady-state gusts still introduce large loads at the root, hence introducing the roll-off is rational.

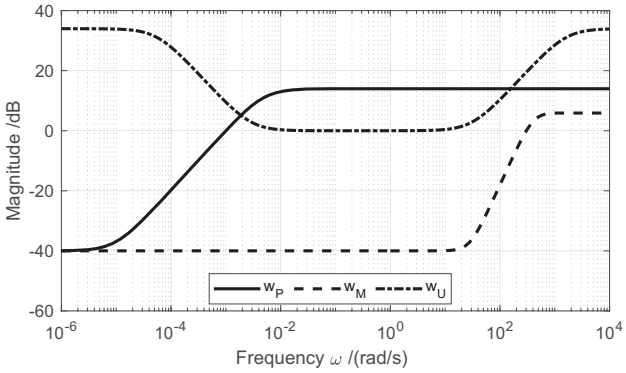

FIG 10. Weighting functions used in H_∞ synthesis

The robustness weight $\mathbf{w}_R$ together with the multiplicative uncertainty [35] weight $\mathbf{w}_M$ is used to take care of the uncertainties occurring in the modeling. In frequency regions with large uncertainty these weights should be high, leading to less aggressive control activity and thereby respecting the limits of the model-based controller design. Here, the uncertainty is defined as the error between full and reduced order model. Although many other uncertainties occur, these are not yet quantifiable. Ideally, the differences between the model and the real wind tunnel wing should be captured. However, real data is not available at this time.
The multiplicative uncertainty weight forms an envelope around the relative error in singular values between full and reduced order model, as presented in figure 7. More details can be found in [35]. The robustness weight can be chosen as an identity matrix. Here, it is chosen to include a roll-off to very large frequencies, in which the controller will not be active. The value of the scalar d added to all measurement channels allows to balance performance and robustness.
The control activity weight $\mathbf{w}_U$ is shaped like a bandstop filter. A certain range of frequencies in which the controller shall be active is penalized less. Low frequencies are penalized more to avoid steady-state deflection of the control surfaces, high frequencies are penalized more to avoid too fast control commands that the actuators cannot provide.

5.3. H_∞ synthesis

Using the generalized plant - which has to be normalized in order to ensure inputs and outputs of similar order of magnitude - the controller can be synthesized following the H_∞ algorithm as detailed in [36]. The aim is to shape the closed loop H_∞ norm such that the control requirements are met, based on the open loop norm. The closed loop norm is determined by a lower linear fractional transform (LFT), $\|\mathbf{F}_l(\mathbf{P}, \mathbf{K})\|_\infty$. Iteratively updating the weights and thereby changing the open loop H_∞ norm, finally the desired closed loop norm is achieved, meeting the desired control targets from section 5.1. The final result is shown in figure 11, where open and closed loop H_∞ norm are presented together with the minimum value γ_{min}, indicating the frequency range in which the closed loop norm could not be minimized any further.
The H_∞ norm of the closed loop is successfully reduced below the one of the open loop in the frequency range from 0.01 to 70 rad/s. This is the frequency range important for GLA, as gusts primarily excite this range. It shall be noted that discrete $1\text{-}cos$ gusts do not excite a distinct frequency - like a continuous sinusoidal gust would - but a large spectrum especially towards lower frequencies. Figure 11 also shows that the first eigenmode occurring at about 55 rad/s

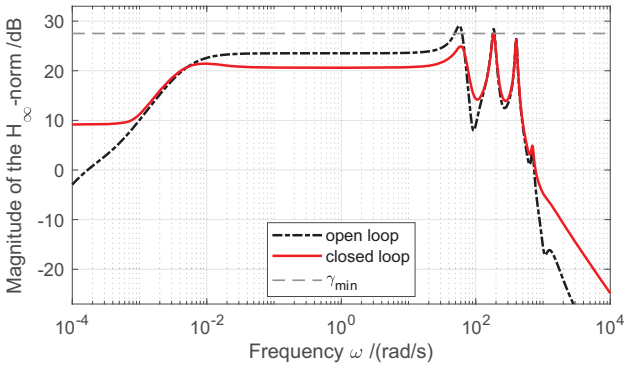

FIG 11. Open and closed loop H_∞ norm

is reduced in magnitude. The second and third peak are reduced as well, while in-between the peaks the closed loop norm is higher. Below 0.01 and above 500 rad/s the roll-off in the weights and the plant allows for the closed loop norm to be above the open loop norm. This gives room for the reduction in the important frequency area. The norm cannot be decreased everywhere, as explained by the waterbed effect [35].
Figure 12 details how the open loop norm is composed. The norm from the gust input to the first and second exogenous output is shown, as well as the overall norm. In the lower frequency regime the overall norm is driven by the performance output, while the upper frequency regime is driven by the robustness output. This demonstrates the frequency separation between the different control targets.

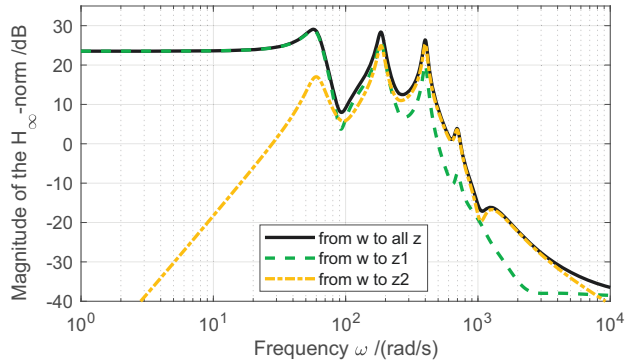

FIG 12. Open loop H_∞ norm, separated by the outputs

6. RESULTS

The designed gust load alleviation is evaluated in the nonlinear simulation with the full order model, in which saturation of the actuators, delay and possibly noise is included. The rigid body motion is set to a steady-state angle of attack of 3°, representing a cruise like configuration. The overall delay in the servo loop is 8 ms [27], the saturation is at 10°, 1129°/s and 75000°/s², for actuator deflection, rate and acceleration, respectively [26]. The nonlinear model is used for time domain simulations. The frequency response is evaluated in the full order linear state-space model.

6.1. Performance Evaluation

The performance of the gust load alleviation can be quantified by comparing the wing-root bending and torsion moment due to a gust with and without controller. Figure 13 presents the time response in WRBM when a gust with a gradient of 3 m acts upon the wing. The steady-state bending moment that is present stems from the 3° angle of attack. The maximum load is successfully reduced, the peak with GLA is 12% lower compared to no GLA, when referring to the absolute level. When referring to the steady-state load level, the relative reduction is 19%. It is worth noting the WRBM is lower with GLA than without it for the entire time, also during the oscillations following the largest peak.

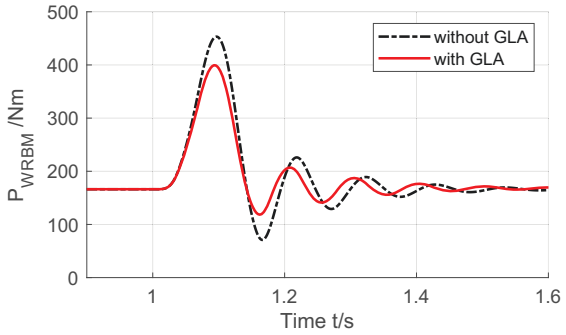

FIG 13. Wing-root bending moment time response for H = 3m

The time response in wing-root torsion moment is presented in figure 14. The torsion moment is reduced as well, by about 31% for the maximum occurring moment. The WRTM is not causing too much concern, because the structural properties of the swept wing have a positive impact on this moment. As the control surfaces are deflected to reduce the bending moment, this creates a torsion moment counteracting the moment occurring in the open loop.

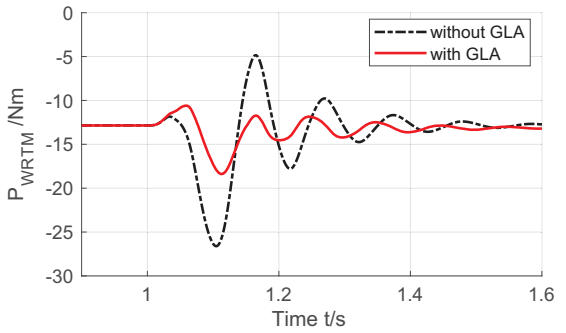

FIG 14. Wing-root torsion moment time response for H = 3m

For both bending and torsion moment it is confirmed that not only the integral loads at the wing root are minimized, but also the local cut loads across the span. The local loads are not exceeding the ones of the open loop.
The reduction in positive bending moment (first, largest peak) is achieved by deflecting the control surfaces upwards. This reduces the lift generated by the wing by adding negative camber, thereby reducing the bending moment. Figure 15 shows the commanded deflection of the five trailing edge control surfaces, output of the controller due to the sensed acceleration. The control surfaces are commanded to deflect quite similar. The difference is due to the size and position of the surfaces. The maximum deflection does not exceed 6°, meaning the saturation is not reached. The same holds for rate and acceleration of the actuators. The number of control surfaces on the wing is the reason for the moderate deflection of the each surface. In a setup with less surfaces, for example only two ailerons on the outer part of the wing, the deflection of each control surface would have to be larger to achieve the same load reduction.

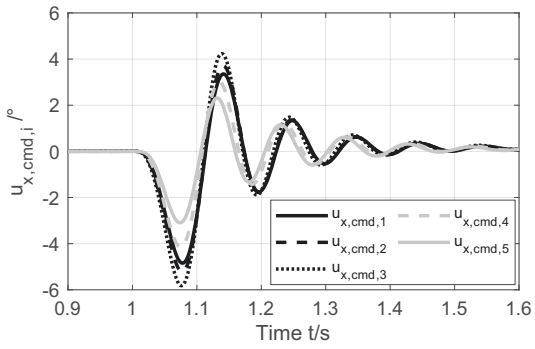

FIG 15. Commanded control surfaces for H = 3m

The GLA should work not only for a certain gust length, like 3 m, but for the entire range of gust gradients required by the certification specification. Analysis shows a very similar relative reduction for various gust gradients H, as depicted in table 1. The absolute reduction in maximum WRBM is different since the WRBM itself is different. The relative reduction based on the overall load level is about 12%, based on the steady-state load level it is about 19%.

TAB 1. Influence of the gust length on bending load reduction

H /m	max. WRBM /Nm		Δ /Nm	δ
	w/o GLA	w/ GLA		
2.0	380	340	-40	-11% (-19%)
3.0	453	400	-53	-12% (-19%)
4.0	480	420	-60	-13% (-19%)
5.0	486	427	-59	-12% (-18%)

The performance of the GLA functionality can also be evaluated in the frequency domain, using the full order linear state-space model. Figure 16 shows the frequency response function from the gust input to the WRBM, again comparing the case with and without GLA. This figure is very similar to figure 11, but this time only one transfer path is examined. As expected, the bending moment is reduced in the relevant frequency range, especially at the peak of 55 rad/s. The wide frequency range of reduced magnitude confirms that the GLA works for a range of gust gradients, as previously discussed.

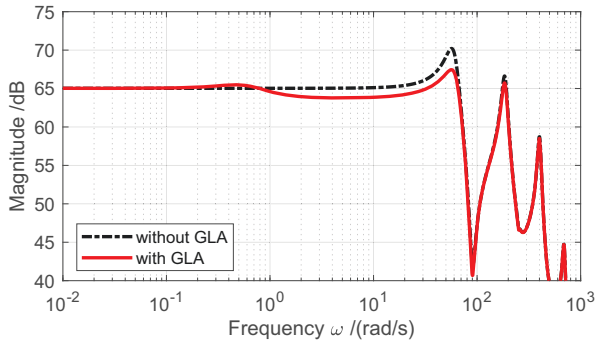

FIG 16. Frequency response from gust w^G to WRBM

The frequency domain also offers an analysis of the controller transfer function, which is mapping between measured accelerations and commanded control surface deflections. When combined with the sensor dynamics, figure 17 results. This figure presents the transfer function between gust excitation and control commands.
The peak in the transfer function occurs at the frequency of the first bending, at approx. 55 rad/s. This means that the controller aims to reduce this peak the most, in order to alleviate the loads. Towards high frequencies a roll-off can be observed, stemming from the actuator dynamics. As noted before, the controller is active in a wide frequency band, ranging down to 0.01 rad/s.

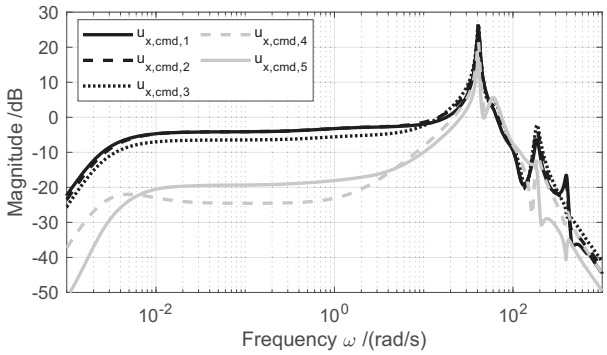

FIG 17. Freq. response from gust w^G to commands $u_{x,cmd,i}$

What is not shown here is the isolated transfer function of the controller, from accelerations to control commands. As the acceleration sensors feature a higher magnitude output towards high frequencies (high-pass characteristic), the controller transfer function exhibits a high gain in the lower frequency range, to restore the observability. This is not ideal and should be investigated in future work.

6.2. Effect of Time Delay and Noise

Time delay in the closed loop system presents a major challenge for the GLA. Based on [26] and [27], it is assumed that the combined delay of sensors, actuators and controller is 8 ms. Without any delay, the performance could be significantly increased. This is shown in figure 18. The dotted line shows the maximum achievable performance without any delay, yielding a 33% reduction in maximum WRBM, based on the steady-state level of loads. When the 8 ms delay is introduced, the performance has to be reduced. Otherwise the oscillations with GLA following the maximum WRBM are larger than the one without GLA. The performance weight has to be reduced by about 40% to regain the desired behavior following a gust excitation. When the delay exceeds 10 ms the closed loop system even becomes unstable. This stresses the importance to keep the delay in the servo loop as small as possible.

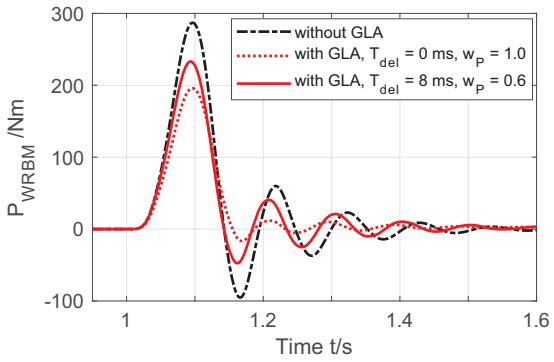

FIG 18. Effect of time delay on the closed loop system

Besides delay, measurement noise is an important aspect to consider. The controller shall work even if some noise is present. Noise with zero mean and a standard deviation of $\sigma = 0.1$ is introduced in the nonlinear simulation. The

effect on the WRBM time response is shown in figure 19. The controller still successfully reduces the wing-root loads. Due to the introduced noise, the controller commands some actuator deflections, leading to the slight deviations around the equilibrium load level.

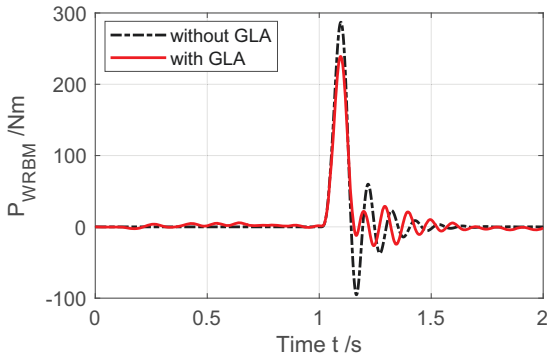

FIG 19. WRBM time response with measurement noise

6.3. Robustness Evaluation Using Disk Margins

Lastly, the robustness of the designed controller is investigated. Disk-based stability margins - both multiloop margins (ML) and loop-at-a-time margins (DL) - [37] are used for this task. The calculations are performed both for the input and output open loop. The disk margins in gain and phase are presented in table 2. The loop-at-a-time margins present the worst case among all possible loops.

TAB 2. Disk-based margins of the open loop transfer function

Type	Cut point	Disk-based gain margin	Disk-based phase margin	Freq.
ML	input	0.57 | 1.76	-30.9° | 30.9°	76 rad/s
ML	output	0.91 | 1.1	-4.8° | 4.8°	55 rad/s
DL	input	0.47 | 2.09	-38.9° | 38.9°	82 rad/s
DL	output	0.76 | 1.32	-15.6° | 15.6°	55 rad/s

The multiloop margins (ML) are always lower than the loop-at-a-time margins (DL). This is due to their more conservative nature, assuming variations in all input or output channels at the same time [37]. The worst case loop-at-a-time margins occurs for the first actuator when considering the input open loop, and for the second acceleration sensor when considering the output open loop. The output margins are more constraining than the input margins.
The multiloop output margins are very small, leaving only 0.1 variation in gain and 5° in phase acceptable. However, these very small margins only occur at the frequency of 55 rad/s, where the controller exhibits the highest action trying to reduce the peak in the frequency response due to the first bending (see figure 17). In other frequency regimes, the margins are significantly bigger. This becomes evident when taking a look at figure 20, in which the multiloop output margin is plotted over frequency. The nominal controller is shown with a solid line.
Figure 20 not only shows the multiloop output margins for the nominal controller, but also for a controller that is performance optimized (dash-dotted line), and one that is robustness optimized (dotted line). In the robustness optimized case, gain and phase margins are increased in the entire frequency range, with the lowest margin still at the frequency of the first bending. In the performance optimized case the stability margins are decreased. Especially the range from 60 to 200 rad/s is concerning, since the controller will still be active in this frequency range and the modeling uncertainty is large, leading to a controller not as effective as desired in the real wind tunnel experiment.

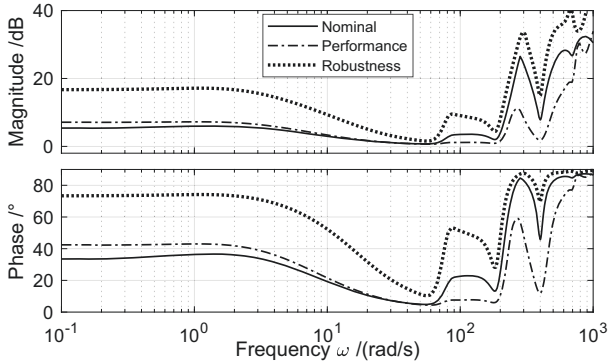

FIG 20. Multiloop output disk margins for different cases

Figure 20 stresses the importance of a careful trade-off between performance and robustness. For a successful deployment of the developed GLA controller in the wind tunnel experiment, the controller needs to be capable to deal with disturbances, delays and unmodeled dynamics. Robustness is also a key requirement since the controller will be discretized for implementation on hardware.

7. SUMMARY AND OUTLOOK

A gust load alleviation controller is designed for the wind tunnel model of a flexible wing, representative for the wing of a long-range transport aircraft. A model-based design using H_∞ robust optimal control is applied. The application of the Loewner framework for gust modeling and model order reduction produces very satisfactory results, allowing to identify state-space models from frequency domain data and reducing their order. Thus, the Loewner framework is a beneficial addition to the aeroservoelastic modeling.
The developed controller is able to reduce the wing-root bending moment due to a gust disturbance by up to 19%, compared to the load level in steady-state flight. The five control surfaces need to deflect by a maximum of 6° to achieve this reduction, which is below their maximum possible deflection. Due to the setup of the generalized plant it is easy to trade-off between performance and robustness by adapting the parameter d.
The H_∞ control strategy proves helpful to incorporate robustness requirements into the controller design, and allows to shape the frequency response of the closed loop system as desired. A downside for MIMO systems is that everything is fused into the maximum singular value (the H_∞ norm), leaving litte insight into the different contributions of the system. The selection of the weighting functions is quite tedious, and the resulting controller is very sensitive to the weight selection. Another aspect noted during design is that slow-moving control surfaces might appear, meaning the surfaces only slowly return to their neutral position. This is undesirable and could possibly be avoided by a time domain based method like LQR, or by a different selection of the weighting functions. This aspect will be addressed in future work.
The upcoming steps will involve a discretization of the controller for use on hardware. Robustness of the discretized controller will be a focus. The oLAF wind tunnel experiment is planned for spring 2024. The insights gained within this project will help to develop gust load alleviation functionalities for next generation transport aircraft.

Contact address:

Felix Stalla, felix.stalla@dlr.de
Research Associate at the Institute of System Dynamics and Control of the German Aerospace Center (DLR)

Acknowledgments:

§ DLR-AE-LAE is the Institute of Aeroelastics, Department Loads Analysis and Aeroelastic Design of the German Aerospace Center (DLR). The structural model, CAD model, as well as the aerodynamic discretization is supplied by this institute. The point of contact is Johannes Dillinger, research associate at said department.

† The oLAF reference configuration is the outcome of a multidisciplinary design optimization. It is detailed in the paper of Wunderlich [4]. The oLAF wind tunnel model is derived from this configuration and defined by Dillinger in [5].

References

[1] Jia Xu and Ilan Kroo. Aircraft design with maneuver and gust load alleviation. *29th AIAA Applied Aerodynamics Conference*, 2022. DOI: 10.2514/6.2011-3180.

[2] Simon Binder. *Simultaneous Optimisation of Composite Wing Structures and Control Systems for Active and Passive Load Alleviation*. PhD thesis, Delft University of Technology, 2021. DOI: 10.4233/uuid:fac93ccf-7e0b-4971-a797-d2617e378a1d.

[3] Markus D. Krengel and Martin Hepperle. Gust and maneuver load alleviation in conceptual overall aircraft design. *AIAA Aviation 2023 Forum*, 2023. DOI: 10.2514/6.2023-3369.

[4] Tobias F. Wunderlich. Multidisciplinary optimization of flexible wings with manoeuvre load reduction for highly efficient long-haul airliners. *2022 Deutscher Luft- und Raumfahrtkongress (DLRK)*, 2022. DOI: 10.25967/570055.

[5] Johannes Dillinger. oLAF Meilensteinbericht M-3.3, Konfiguration für LA-Demonstratorexperiment. Technical report, internal, German Aerospace Center (DLR), 2022.

[6] J. Hofstee, T. Kier, C. Cerulli, and G. Looye. A variable, fully flexible dynamic response tool for special investigations (VarLoads). *International Forum on Aeroelasticity and Structural Dynamics (IFASD)*, 2003.

[7] Thiemo M. Kier and Jeroen Hofstee. VarLoads - eine Simulationsumgebung zur Lastenberechnung eines voll flexiblen, freifliegenden Flugzeugs. *2004 Deutscher Luft- und Raumfahrtkongress (DLRK)*, 2004.

[8] A.J. Mayo and Athanasios C. Antoulas. A framework for the solution of the generalized realization problem. *Linear Algebra and its Applications*, 425, 2007. DOI: 10.1016/j.laa.2007.03.008.

[9] Thiemo Kier and Gertjan Looye. Unifying manoeuvre and gust loads analysis models. *International Forum on Aeroelasticity and Structural Dynamics (IFASD)*, 2009.

[10] Christian Reschke. *Integrated Flight Loads Modelling and Analysis for Flexible Transport Aircraft*. PhD thesis, University of Stuttgart, 2006. DOI: 10.18419/opus-3733.

[11] William P. Rodden and Erwin H. Johnson. *MSC/NASTRAN Aeroelastic Analysis User's Guide*. MSC, 2nd edition, 1994. ISBN: 978-1-585-24006-7.

[12] European Union Aviation Safety Agency. Certification specification and acceptable means of compliance for large aeroplanes (CS-25), Amendment 27. Technical report, 2023.

[13] Robert J. Guyan. Reduction of stiffness and mass matrices. *AIAA Journal*, 3(2), 1964. DOI: 10.2514/3.2874.

[14] Michel Géradin and Daniel J. Rixen. *Mechanical Vibrations, Theory and Applications To Structural Dynamics*. Wiley, 3rd edition, 2015. ISBN: 978-1-118-90020-8.

[15] Max Blair. A compilation of the mathematics leading to the doublet lattice method. Final report ADA256304, Air Force Wright Laboratory, 1992.

[16] Edward Albano and William P. Rodden. A doublet-lattice method for calculating lift distributions on oscillating surfaces in subsonic flows. *AIAA Journal*, 7(2), 1969. DOI: 10.2514/3.5086.

[17] Wolfgang Geißler. Verfahren in der instationären Aerodynamik. Technical report, DLR-FB 93-21, German Aerospace Center (DLR), 1993.

[18] Raymond L. Bisplinghoff, Holt Ashley, and Robert L. Halfman. *Aeroelasticity*. Dover Publications Inc., 2nd edition, 1983. ISBN: 978-1-621-98657-7.

[19] Tobias Mauermann. Flexible aircraft modelling for flight loads analysis of wake vortex encounters. Technical report, DLR-FB 2010-37, German Aerospace Center (DLR), 2011. DOI: 10.24355/dbbs.084-201109120959-0.

[20] Armin Beckert and Holger Wendland. Multivariate interpolation for fluid-structure-interaction problems using radial basis functions. *Aerospace Science and Technology*, 5(2), 2001. DOI: 10.1016/S1270-9638(00)01087-7.

[21] Kenneth L. Roger. Airplane math modeling methods for active control design. *AGARD Conference Proceedings 228, AGARD-CP-228*, 1977.

[22] Mordechay Karpel. Design for active flutter suppression and gust alleviation using state-space aeroelastic modeling. *AIAA Journal*, 19(3), 1982. DOI: 10.2514/3.57379.

[23] Jan R. Wright and Jonathan E. Cooper. *Introduction to Aircraft Aeroelasticity and Loads*. Wiley, 2nd edition, 2015. DOI: 10.1002/9781118700440.

[24] C. Fielding and P. K. Flux. Non-linearities in flight control systems. *The Aeronautical Journal*, 107, 2003. DOI: 10.1017/S0001924000013543.

[25] Manuel Pusch, Daniel Ossmann, Johannes Dillinger, Thiemo M. Kier, Martin Tang, and Jannis Lübker. Aeroelastic modeling and control of an experimental flexible wing. *AIAA Scitech 2019 Forum*, (AIAA 2019-0131), 2019. DOI: 10.2514/6.2019-0131.

[26] Martin Tang, Marc Böswald, Yves Govers, and Manuel Pusch. Identification and assessment of a nonlinear dynamic actuator model for controlling an experimental flexible wing. *CEAS Aeronautical Journal*, 12, 2021. DOI: 10.1007/s13272-021-00504-y.

[27] Manuel Pusch. *Blending of Inputs and Outputs for Modal Control of Aeroelastic Systems*. PhD thesis, Hamburg University of Technology (TUHH), 2020. https://elib.dlr.de/139100/.

[28] David Quero, Christoph Kaiser, Pierre Vuillemin, and Charles Poussot-Vassal. A state-space model for loads analysis based on tangential interpolation. *IFASD 2019 Conference Proceedings*, 2019.

[29] Hugo Fournier, Paolo Massioni, Minh Tu Pham, Laurent Bako, Robin Vernay, and Michele Colombo. Robust gust load alleviation of flexible aircraft equipped with lidar. *Journal of Guidance, Control, and Dynamics*, 45(1), 2022. DOI: 10.2514/1.G006084.

[30] Dimitrios S. Karachalios, Ion Victor Gosea, and Athanasios C. Antoulas. *Model Order Reduction: The Loewner framework for system identification and reduction*, chapter 6, pages 181–228. De Gruyter, 2021. DOI: 10.1515/9783110498967-006.

[31] Antonio Cosmin Ionita. *Lagrange rational interpolation and its applications to approximation of large-scale dynamical systems*. PhD thesis, Rice University, 2013. https://hdl.handle.net/1911/77180.

[32] M. Köhler. On the closest stable descriptor system in the respective spaces RH_2 and RH_∞. *Linear Algebra and its Applications*, 443, 2014. DOI: 10.1016/j.laa.2013.11.012.

[33] Timo Reis and Tatjana Stykel. Balanced truncation model reduction of second-order systems. *Mathematical and Computer Modelling of Dynamical Systems*, 14(5), 2008.

[34] Peter Brenner and Tobias Breiten. *Model Reduction and Approximation: Model Order Reduction Based on System Balancing*. Society for Industrial and Applied Mathematics, 2017. DOI: 10.1137/1.9781611974829.ch6.

[35] Sigurd Skogestad and Ian Postlethwaite. *Multivariable Feedback Control*. John Wiley & Sons, 2nd edition edition, 2005. ISBN: 978-0-470-01168-3.

[36] John C. Doyle, Keith Glover, Pramod P. Khargonekar, and Bruce A. Francis. State-space solutions to standard H_2 and H_∞ control problems. *IEEE Transactions on Automatic Control*, 34(8), 1989. DOI: 10.1109/9.29425.

[37] Peter Seiler, Andrew Packard, and Pascal Gahinet. An introduction to disk margins [lecture notes]. *IEEE Control Systems Magazine*, 40, 2020. DOI: 10.1109/MCS.2020.3005277.